# High density hydrogen storage in superactivated carbons from hydrothermally carbonized renewable organic materials

M. Sevilla[a,b], A. B. Fuertes[a], R. Mokaya[b*]

[a] Instituto Nacional del Carbón (CSIC), P.O. Box 73, 33080 Oviedo, Spain

[b] School of Chemistry, University of Nottingham, University Park, Nottingham NG7 2RD, U. K.

[*] Corresponding author. Fax: +44 115 9513562. E-mail address: r.mokaya@nottingham.ac.uk (R. Mokaya)

**Abstract**

Hydrothermally carbonized organic materials (furfural, glucose, starch, cellulose and eucalyptus sawdust) have been used as precursors to produce high-surface area carbons. The synthesis methodology comprises two steps: i) hydrothermal carbonization of organic materials and ii) chemical activation with KOH as activating agent. In this way, activated carbon materials with a high surface area (up to 2700 $m^2$ $g^{-1}$) and narrow micropore size distribution in the supermicropore range (0.7 - 2 nm) are produced. The textural properties of the activated carbon products can be easily tuned by modifying the activating conditions (i. e., activation temperature and the amount of KOH used). The activated carbon materials exhibit high hydrogen uptakes, up to 6.4 wt%, and large isosteric heats of adsorption, up to 8.5 kJ $mol^{-1}$. In particular, the hydrogen storage density of the carbons is high and ranges between 12 and 16.4 μmol $H_2 \cdot m^{-2}$. The hydrogen storage density is closely related to the pore size of the carbons, with small micropores (ca. 1 nm) favouring a high density. Taking into account the high hydrogen storage capacities of these materials, as well as the simplicity of their synthesis procedure and the ready availability and low-cost of the raw precursors, it can be concluded that these activated carbons constitute a promising adsorbent for hydrogen storage.

## Broader context

Hydrogen storage is widely-known to be a limiting step for achieving a hydrogen-based economy. In spite of the research efforts, up to date there is no material capable of storing enough amount of hydrogen to accomplish the targets established by the US DOE for on-board applications. Porous carbon materials are among the main candidates for hydrogen storage due to their relatively low cost, high surface area, large pore volume and ability to design their pore structure. In this manuscript we report on the preparation of activated carbons from hydrothermally carbonized substances by a low time consuming chemical activation process with KOH. The activated carbons possess high surface areas (up to 2700 $m^2\ g^{-1}$) and narrow pore size distributions in the supermicropore range (0.7 - 2 nm). The textural properties of the activated carbon products can be easily tuned by modifying the activating conditions (i. e., activation temperature and the amount of KOH used). The activated carbon materials exhibit high hydrogen uptakes, up to 6.4 wt% (20 bar and -196ºC), and large isosteric heats of adsorption, up to 8.5 kJ $mol^{-1}$. In particular, the hydrogen storage density of the carbons is high (12 - 16.4 μmol $H_2 \bullet m^{-2}$) and closely related to the pore size of the carbons, with small micropores (ca. 1 nm) favouring a high density.

## 1. Introduction

In the last few years the process of hydrothermal carbonization, i.e., heat treatment of an aqueous solution/dispersion of an organic material such as saccharides (glucose, sucrose, starch or cellulose), simpler compounds such as furfural or more complex substances such as biomass, at temperatures in the range 150 – 350ºC under autogeneous pressure, has received increasing attention.[1] This is due to several reasons: i) the precursors are readily available, cheap and renewable (i.e., saccharides or biomass), ii) it is a "green" and simple process as it only involves water as solvent and consists of a simple heat-treatment in a closed autoclave and iii) the resulting solid carbon products exhibit attractive chemical and structural properties. The solid products, which are termed hydrochar, are composed of spherical microparticles, whose size can be tuned by modifying the operating conditions (i.e., temperature, solution concentration, reaction time and precursor).[1-3] These microparticles consist of small clusters of condensed aromatic structures, along with some aliphatic/hydroaromatic structures, bearing a high concentration of oxygen groups. The oxygen groups in the core are stable functionalities, whereas those in the shell are more reactive/hydrophilic.[2,3] These chemical and physical properties make this material suitable as sacrificial template for the fabrication of hollow spheres of inorganic materials ($Ga_2O_3$, GaN, $WO_3$, $SnO_2$, etc.)[4-8] or for the synthesis of metal/carbon composites.[9] However, the solid product has the drawback of possessing almost no porosity,[2,3] unless it is subjected to additional heat-treatment at higher temperature[10] or synthesized in the presence of a template.[11-13] This restricts its application in adsorption processes such as removal of contaminants or in gas/energy storage. The synthesis of highly porous carbon materials based on the hydrochar products therefore presents a challenge. Porous materials based on hydrochar can be useful in emergent applications such as hydrogen storage or electrical energy storage (supercapacitors).

High temperature treatment of a mixture of raw carbonaceous material and certain chemical agents (e.g., KOH, $H_3PO_4$, $SnCl_2$, etc) is a well-known route to highly porous carbon materials. This process, commonly referred to as chemical activation, gives rise to carbon materials that possess high surface area (> 2000 $m^2$ $g^{-1}$) and a large porosity made up of super-micropores (~ 1 - 2 nm) and small mesopores.[14-17] High surface area microporous carbons have great relevance for potential use as hydrogen stores or as electrode materials in electrochemical capacitors. Both the magnitude of the surface area and the pore size of some chemically activated carbons can be modulated by controlling the activation conditions (i. e., temperature, type and amount of chemical agent, heating rate, impregnation method, etc).[18-20]

Taking into account the chemical characteristics of hydrochar products (i.e., high concentration of oxygen functional groups and low degree of aromatization), it can be envisaged that this type of material may constitute an excellent precursor for the preparation of activated carbons via controlled chemical activation. To the best of our knowledge, this type of material has never been activated before. In this work, we investigate the use of hydrochar as precursor for the preparation of chemically activated carbons. We analysed various types of hydrochar products obtained from a variety of substances: a) biomass (eucalyptus sawdust), b) saccharides (glucose, starch, cellulose) and c) furfural, and investigated how the textural characteristics of the activated carbons can be modulated through variation of the activation conditions (activation temperature and the hydrochar/KOH ratio). Finally, we assessed the use of the chemically activated carbons as adsorbents for hydrogen storage.

## 2. Experimental

### 2.1 *Synthesis of hydrochar materials*

Hydrochar materials were prepared by hydrothermal carbonization of the following substances: α-D-Glucose (96%, Aldrich), potato starch (Sigma-Aldrich), cellulose (Aldrich),

eucalyptus sawdust and furfural (Aldrich). Briefly, an aqueous solution/dispersion of the various materials, at a concentration of 320 g $L^{-1}$ (except for furfural, where 145 g $L^{-1}$ was used), was placed in a stainless steel autoclave and heated up to 230ºC (for glucose and starch) or 250ºC (for cellulose, eucalyptus sawdust and furfural) and maintained at the target temperature for 2 h. The resulting solid product, denoted as hydrochar, was recovered by filtration and washed abundantly with distilled water and then dried at 120ºC for 4 h. The various hydrochar materials are denoted as follows: G = glucose-based hydrochar, S = starch-based hydrochar, C = cellulose-based hydrochar, E = eucalyptus sawdust based-hydrochar and F = furfural-based hydrochar.

### 2.2 *Chemical activation of the hydrochar materials*

The hydrochar materials were chemically activated using potassium hydroxide (Sigma-Aldrich). The cellulose-derived hydrochar was activated at temperatures in the range 600 – 800ºC at hydrochar/KOH weight ratios of 1:2 or 1:4. For the rest of the hydrochar materials, the operational conditions were: 700ºC and a hydrochar/KOH ratio of 1:4. Briefly, the hydrochar was thoroughly mixed with KOH at the desired ratio in an agate mortar and then the mixture was heat treated to the target temperature (heating ramp rate of 3ºC $min^{-1}$) in a horizontal furnace under a nitrogen gas flow and held at the desired temperature for 1 h. The activated samples were then thoroughly washed several times with 10 wt% HCl to remove any inorganic salts, and then washed with distilled water until neutral pH. Finally, the activated carbon was dried in an oven at 120ºC for 3 h. The activated carbons thus synthesized were denoted as X-Y-T, where X is the hydrochar designation as described above, Y is the hydrochar/KOH weight ratio (i.e., 1/2 or 1/4) and T is the activation temperature (in ºC). To differentiate the four activated carbons derived from cellulose, they were denoted (for hydrochar designation, X) as Cn, where n is 1, 2, 3 or 4 depending on the activation conditions.

Two of the cellulose derived activated carbons were subjected to further activation, and the resulting re-activated carbons were designated as ACn (Y-T), where Y is the hydrochar/KOH weight ratio (i.e., 1/2 or 1/4) and T is the activation temperature (in ºC) for the second activation step.

### 2.3 *Characterization*

The morphology of the samples was examined by Scanning Electron Microscopy (SEM) using a Zeiss DSM 942 microscope. Diffuse reflectance infrared (IR) spectra of the powders of the materials were recorded on a Nicolet Magna-IR 560 spectrometer fitted with a diffuse reflection attachment. Nitrogen sorption isotherms and textural properties of the carbons were determined at -196$^{o}$C using nitrogen in a conventional volumetric technique by a Micromeritics ASAP 2020 sorptometer. The surface area was calculated using the BET method based on adsorption data in the partial pressure (P/Po) range 0.04 to 0.2 and total pore volume was determined from the amount of nitrogen adsorbed at a relative pressure of 0.99. Micropore surface area and micropore volume were obtained via t-plot analysis. The characteristic adsorption energy, $E_0$, and the average pore width, $L_0$, were calculated by the analysis of the low pressure data using the Dubinin-Radushkevich equation[21] and the equation proposed by Stoeckli[22] respectively. The pore size distribution (PSD) was determined via a Non Local Density Functional Theory (NLDFT) method using nitrogen adsorption data, and assuming a slit pore model.

**Hydrogen uptake measurements**: Hydrogen uptake capacity of the carbons was measured by gravimetric analysis with an Intelligent Gravimetric Analyser, IGA, (Hiden) using 99.9999% purity hydrogen additionally purified by a molecular sieve filter. The hydrogen uptake measurements were performed at -196$^{o}$C (in a liquid nitrogen bath) over the pressure range 0 to 20 bar. With the purpose of calculating the isosteric heat of adsorption, hydrogen uptake measurements were also performed at -186ºC (in a liquid

argon bath) over the pressure range 0 – 20 bar. The uptake data was corrected for the buoyancy of the system and samples. The hydrogen uptake was calculated on the basis of a density of 1.5 g/cm$^3$ for the carbons.

## 3. Results and Discussion

### 3.1 *Structural and chemical properties of the hydrochar materials and activated carbons*

A schematic representation of the overall synthesis procedure of the superactivated carbons is depicted in Figure 1. It comprises two simple steps: 1) hydrothermal carbonization of saccharides (glucose, starch and cellulose), furfural or biomass (eucalyptus sawdust), which gives rise to a carbon-rich solid called hydrochar and 2) chemical activation of the obtained hydrochars with KOH as activating agent.

Our previous work has shown that hydrochar materials derived from glucose, starch and cellulose are composed of agglomerates of spherical particles of size in the micron range.[2,3] This is illustrated, for the present materials, in Figures 2a and 2b. For the furfural-derived hydrochar, the SEM image displayed in Figure 2c shows that the morphology is similar to that of mono/polysaccharides. However, in the case of the eucalyptus sawdust-derived hydrochar, Figure 2d reveals that the particles retain the cellular appearance of the raw material, although they are covered by microspheres, which are probably generated as a consequence of the transformation of the cellulosic fraction.[3] From a chemical point of view, these materials possess a high concentration of oxygen groups, as evidenced by the elemental chemical analysis given in Table 1. The O/C atomic ratios of the hydrochars (ca. 0.26) in Table 1 are in the typical range (i.e., O/C atomic ratio of 0.2 – 0.4) previously reported.[2,3] As illustrated in Figure 1, the chemical hydrochar model structure consists of small clusters of condensed benzene rings that form stable groups with oxygen in the core (i.e., ether, quinone, pyrone), whereas the shell possesses more reactive/hydrophilic oxygen functionalities (i.e., hydroxyl, carbonyl, carboxylic, ester).[2,3] The oxygen functional groups can be identified by

infrared spectroscopy. As an example, the FT-IR spectra of the cellulose and eucalyptus sawdust-derived hydrochars with the corresponding peak assignments are shown in Figure S1 (Supporting Information). The chemical structure and morphology of the hydrochars are the result of the following reactions: (i) hydrolysis of the organic substrate, (ii) dehydration and fragmentation into soluble products of the monomers that come from the hydrolysis process, (iii) polymerization or condensation of the soluble products, (iv) aromatization of the polymers thus formed, (v) appearance of a short burst of nucleation and (vi) growth of the nuclei so formed by diffusion and linkage (through the reactive oxygen functionalities) of species from the solution to the surface of the nuclei.[2,3] The high functionalization of the hydrochar, as well as its low condensation degree, make this material a good precursor for the chemical activation process, as these characteristics make the hydrochar highly reactive and the reactivity of the precursor is a key parameter in the activation process.[20,23]

For temperatures < 700ºC, the reactions between the activating agent (KOH) and the carbonaceous materials (hydrochar) consist of solid-solid or solid-liquid processes that occur through the following stoichiometric redox reaction:[24,25]

$$6\ KOH + 2\ C \leftrightarrow 2\ K + 3\ H_2 + 2\ K_2CO_3 \quad (1)$$

For temperatures higher than 700ºC, decomposition of $K_2CO_3$ takes place:[18,26]

$$K_2CO_3 \leftrightarrow K_2O + CO_2 \quad (2)$$

Several studies have shown that the higher the reactivity of the precursor, the lower the temperature required to trigger reaction (1),[20,23] the higher the degree of gasification caused by the $CO_2$ evolved from $K_2CO_3$ according to reaction (2) and the larger the resultant porosity development.[18]

The activated carbons exhibit morphology characterized by irregular shaped particles with large conchoidal cavities and smooth surfaces, as shown by the SEM images of E-1/4-700 (Figure 2e) and C1-1/4-600 (Figure 2f) samples. This morphology was found to be

common for all activated samples regardless of the hydrochar precursor, thereby suggesting that a drastic morphological transformation takes place during the activation process. This indicates that the activated carbons retain no memory of the structure of their parent hydrochar. Regarding their chemical composition, in relation to the hydrochar samples, a large decrease in the O/C atomic ratio is registered (see Table 1). Thus, the O/C values are < 0.06, except for the sample activated at the lowest temperature (i.e., sample C1-1/4-600) and that activated at a lower hydrochar/KOH ratio (i.e., sample C4-1/2-700), which have an atomic O/C ratio of ca. 0.1. The decrease in atomic O/C ratio (compared to the precursor hydrochar) is due to heat-treatment of the hydrochar at a higher temperature, which causes further carbonization and release of oxygenated compounds such as CO and $CO_2$. As expected, increase in activation temperature leads to a decrease of the O/C ratio: $(O/C)_{C1\text{-}1/4\text{-}600}$ (0.099) > $(O/C)_{C2\text{-}1/4\text{-}700}$ (0.057) > $(O/C)_{C3\text{-}1/4\text{-}800}$ (0.035). On the other hand, sample C4-1/2-700 has the highest O/C atomic ratio due probably to the lower amount of KOH used in relation to the rest of the samples and therefore a lower burn-off of the sample, as confirmed by the yield of 48% (Table 2).

### 3.2 *Porous textural characteristics of the activated carbons*

The hydrochar materials possess hardly any porosity; the saccharide and eucalyptus sawdust derived hydrochars have surface area < 4 $m^2\ g^{-1}$, and the cellulose-derived hydrochar exhibits a surface area of ca. 30 $m^2\ g^{-1}$. These surface area values match well with the external surface area determined by the $\alpha_s$-plot technique.[3] Therefore, the hydrochar materials posses virtually no framework-confined pores, and their surface area arises mainly from interparticle voids. However, after chemical activation with KOH, all the hydrochar materials generate porous carbons with highly developed porosity in the supermicropore range and surface areas typically > 2000 $m^2\ g^{-1}$ (Table 2).

The nitrogen sorption isotherms for the cellulose-derived hydrochars activated at various temperatures in the 600 – 800ºC range, at a hydrochar/KOH weight ratio of 1:4, are shown in Figure 3a and the corresponding textural parameters are summarized in Table 2. It can be seen that all the activated samples, regardless of the activation temperature, exhibit a type I isotherm, typical of microporous materials. The microporous character of the materials is confirmed by the value of the characteristic adsorption energy, $E_0$, determined using the Dubinin-Raduskevich equation. All the activated carbons possess values of $E_0 > 16$ kJ·mol$^{-1}$ (Table 2) as expected for microporous materials.[27,28] As the activation temperature increases, there is a widening of the knee of the isotherm, which indicates a broadening of the micropore size distribution, and formation of larger micropores. This is supported by the decrease in the value of the characteristic energy $E_0$ (from 18.3 kJ mol$^{-1}$ at 600ºC to 16.5 kJ mol$^{-1}$ at 800ºC) and the increase of the average pore width $L_0$ (from 1.6 nm at 600ºC to > 2 nm at 800ºC). This widening of the micropore size is also confirmed by the DFT pore size distribution curves shown in Figure 3b. Thus, whereas the sample activated at 600ºC possesses only one pore system centred at 1.2 nm, the samples activated at 700 and 800ºC possess a second pore system at 1.5 nm for the former and 2.0 nm for the latter. This result reveals an enlargement of the pore size as the activation temperature increases. This widening of the pore distribution with the activation temperature is related to gasification of the hydrochar precursor by the $CO_2$ evolved in the decomposition of the $K_2CO_3$ generated in the activation process for temperatures higher than 700ºC.[18,24,26] The gasification of the hydrochar precursor as the temperature rises is confirmed by the decrease in the yield at higher activation temperature (Table 2).

The nitrogen sorption isotherms in Figure 3a show that there is an upward shift in adsorption (i.e., an increase in overall porosity) when the activation temperature increases from 600 to 700ºC. The surface area and total pore volume increase from 2014 m$^2$ g$^{-1}$ and

0.94 $cm^3$ $g^{-1}$ at 600ºC to 2370 $m^2$ $g^{-1}$ and 1.08 $cm^3$ $g^{-1}$ at 700ºC. A further increase in activation temperature from 700 to 800$^o$C, however results in a decrease in porosity to levels comparable to activation at 600$^o$C. The surface area (2047 $m^2$ $g^{-1}$) and pore volume (0.98 $cm^3$ $g^{-1}$) of the sample activated at 800$^o$C are lower than for the 700$^o$C sample. The samples activated at 600 and 700ºC possess a similar proportion of microporosity with 92 – 95% of their surface area and 85 – 91% of pore volume arising from micropores. For the sample activated at 800$^o$C, the proportion of microporosity is lower at 83% of surface area and 76% of pore volume. The porosity data suggest that the optimum activation temperature for the cellulose based hydrochar materials is ca. 700ºC. Similar trends, on the effect of activation temperature, have previously been reported for other types of carbon precursors.[29,30] When the cellulose-derived hydrochar is activated at 700$^o$C using a hydrochar/KOH weight ratio of 1/2 instead of 1/4, the resulting activated carbon exhibits lower porosity as shown by the isotherm in Figure 3a and textural parameters in Table 2. Indeed, the nitrogen uptake of sample C4-1/2-700 is almost half that of C2-1/4-700, with the consequence that the surface area and pore volume of the former are about half those of the latter.

The pore size distribution (PSD) curves shown in Figure 3b indicate that activated carbons obtained by using small amounts of activating agent (hydrochar/KOH ratio of 1/2) exhibit narrower PSD and smaller micropores compared to the samples prepared at KOH hydrochar/KOH ratio of 1/4. Thus, the PSD of sample C4-1/2-700 is centred at ca. 0.9 nm and no pores above 2 nm are observed (Figure 3b). The presence of smaller pores is supported by the value of $E_0$ and $L_0$ (22.3 kJ $mol^{-1}$ and 1.0 nm, respectively). The generation of a wider PSD for carbons activated at hydrochar/KOH ratio of 1/4 is due to the greater formation of $K_2CO_3$ and hence more $CO_2$ is generated leading to higher gasification of the

carbon.[18,24,26] This explanation is consistent with the decrease in carbon yield as the amount of KOH used increases (Table 2).

Taking into account the results described above for the cellulose-derived activated carbons, the other hydrochar samples (from glucose, starch, furfural and sawdust) were activated at 700ºC using a hydrochar/KOH ratio of 1/4. The nitrogen sorption isotherms for these samples are shown in Figure 4a. It can be clearly seen that, regardless of the type of hydrochar used as precursor, all the resulting activated carbons exhibit the same shape of isotherm, which suggests similar textural characteristics. This is confirmed by the textural parameters in Table 2. The samples possess similar pore volume of ca. 1.0 $cm^3$ $g^{-1}$, and surface area of ca. 2200 $m^2$ $g^{-1}$ except for the activated carbon prepared from cellulose-derived hydrochar which has a slightly higher surface area and pore volume, i.e. 2370 $m^2$ $g^{-1}$ and 1.08 $cm^3$ $g^{-1}$. The samples have comparable proportion of micropore surface area (93 – 95%) and micropore volume (85 – 91%). Furthermore, all the samples have similar values of $E_0$, between 17.3 and 18.3 kJ $mol^{-1}$, and $L_0$ in the 1.6 - 1.8 nm range. The pore size distribution of the samples, given in Figure 4b, shows a bimodal pore size distribution, centred at 1.2 and 1.5 nm. In all the samples, the population of the smaller pore size is slightly higher than that of the larger one, except for the activated carbon derived from eucalyptus sawdust-derived hydrochar, where the population of both pore size systems is the same. These results indicate that, regardless of the type of hydrochar used, the activated carbons generated exhibit similar textural characteristics. This may be related to the fact that, as shown by the SEM images (Figure 2e and 2f), the activated carbons retain no memory of the structure of their parent hydrochar.

Overall, the porosity data shows that hydrochar materials constitute an excellent precursor for the synthesis, via chemical activation with KOH, of carbon materials with high surface area (up to 2400 $m^2$ $g^{-1}$) and relatively narrow PSDs centred in the supermicropore range. The

chemical activation with KOH greatly enhances the textural properties of the hydrochar materials thereby potentially broadening their fields of application. Additionally, it is clear that varying the operating conditions (i.e., activation temperature and hydrochar/KOH weight ratio) permits some control over the textural properties. Specifically, the size of the micropores can be tuned between 1 and 2 nm by modifying the carbonization temperature and the amount of activating agent. This is illustrated in Figure 3b for the cellulose-derived activated carbons. A further attraction of the present synthesis route is that the precursors used are readily available, and can be obtained via an environmentally friendly (green) and sustainable process (i.e. hydrothermal carbonization). It is worth emphasizing that the use of eucalyptus sawdust provides particular advantages (even when compared to glucose, cellulose, starch and furfural) in view of the fact that it is readily available and is directly obtained from nature without any need for extraction or processing from biomass.

### 3.3 *Porous textural characteristics of re-activated carbons*

To further fine-tune the textural properties of the activated carbons, we performed the activation of two cellulose derived activated carbons. The effect of the second activation step appears to depend on the re-activation conditions. Re-activation of sample C1-1/4-600 at 600$^{o}$C and a hydrochar/KOH ratio of 1/4, yielding sample AC1(1/4-600) does not have any significant effect on porosity as shown in Figure 5a. The nitrogen sorption isotherm remains largely unchanged except for a slightly smaller adsorption step. The surface area and pore volume only undergo small decreases from 2014 $m^2/g$ and 0.94 $cm^3/g$ to 1853 $m^2/g$ and 0.87 $cm^3/g$ as shown in Table 3. The pore size distribution also remains largely unchanged with a pore size maxima of ca. 1.2 nm as shown in Figure 5b. The unchanging porosity is confirmed by similar $E_0$ (18 – 18.3 kJ $mol^{-1}$) and $L_0$ (1.6 nm) values (Table 3). However, re-activation of sample C1-1/4-600 at 700$^{o}$C and a hydrochar/KOH ratio of 1/4, yielding sample AC1(1/4-700) causes major changes in porosity. The overall porosity significantly increases (Figure 5a)

and new pores of size ca. 2 nm are generated in addition to the original 1.2 nm pores so that the re-activated AC1(1/4-700) sample has a bimodal pore size distribution (Figure 5b). The surface area and pore volume increase to 2722 $m^2/g$ and 1.23 $cm^3/g$. As expected the $E_0$ value decreases to 16.8 kJ $mol^{-1}$ and $L_0$ value increases to 2.0 nm. However, despite the vastly different effects of the two re-activation processes, the proportion of microporosity remains unaffected at 91% of surface area and 85% of pore volume. This means that the main effect of the re-activation step is to alter the micropore size distribution but without generating any larger pores (i.e. mesopores) outside the micropore range.

Re-activation of the rather low surface area sample C4-1/2-700 generated interesting results. Re-activation at 600$^o$C and a hydrochar/KOH ratio of 1/2, yielding sample AC4(1/2-600) does not have any effect on the overall porosity as shown in Figure 6a and Table 3. The nitrogen sorption isotherm remains unchanged (Figure 6a) and the surface area and pore volume remain virtually unchanged at 1280 $m^2/g$ and ca. 0.64 – 0.68 $cm^3/g$, as shown in Table 3. However, the pore size distribution broadens significantly (Figure 6b). The change in micropore size distribution is confirmed by the decrease in the $E_0$ value from 22.3 kJ $mol^{-1}$ to 19.1 kJ $mol^{-1}$ and increase in $L_0$ value from 1.0 nm to 1.4 nm (Table 3). The main effect of the re-activation step is therefore alteration of the micropore size distribution but without any change in the overall textural properties or proportion of microporosity, which remains at ca. 95% of surface area and 83% of pore volume. On the other hand re-activation of sample C4-1/2-700 at 700$^o$C and a hydrochar/KOH ratio of 1/4 to yield sample AC4(1/4-700) causes major increase in porosity (Figure 6a) and new pores of size between 1 and 3 nm are generated; the original 0.9 nm pores do not appear to be retained (Figure 6b). The surface area and pore volume increase to 2469 $m^2/g$ and 1.18 $cm^3/g$. The $E_0$ value decreases from 22.3 kJ $mol^{-1}$ to 16.8 kJ $mol^{-1}$ and in $L_0$ value increases from 1.0 nm to 2.0 nm. This represents a shift in micropore size distribution from 0.9 nm to between 1.2 and 2 nm.

Nevertheless, the proportion of microporosity is only slightly lower at 91% of surface area and 81% of pore volume. Once again the main effect of the re-activation appears to be a modification of the micropore size distribution.

### 3.4 *Hydrogen storage*

Figure 7 shows the dependence of the hydrogen uptake on pressure at -196ºC for the activated carbons produced from the hydrochar samples derived from cellulose (Figure 7a) and the other hydrochar precursors (Figure 7b). All the activated carbons exhibit similar hydrogen uptake isotherms, which show complete reversibility (i.e., no hysteresis). Furthermore, no saturation is achieved in the 20 bar pressure range, which suggests that higher hydrogen adsorption capacity can be achieved by increasing the pressure above 20 bar. The shape of the hydrogen uptake isotherms at -186ºC (liquid argon bath) is similar to those in Figure 7 (Figure S2, Supporting Information) but with lower hydrogen uptake as expected for sorption at higher temperature. The hydrogen storage capacities at 1 and 20 bar are given in Table 2. The hydrogen storage capacity of the activated carbons is in the 2.1 – 2.5 wt% range at 1 bar and 4.2 – 5.6 wt% range at 20 bar. The hydrogen uptakes reported here are in most cases superior to those obtained for other activated carbons with large surface area (in the 1500 – 3200 $m^2 g^{-1}$ range) under similar conditions.[31-36]

The effect of re-activation of the activated carbons on hydrogen storage depends on the reactivation conditions and any subsequent changes in porosity as shown in Figure 8. Re-activation of sample C1-1/4-600 at 600$^o$C and a hydrochar/KOH ratio of 1/4 to yield sample AC1(1/4-600) does not have any significant effect on hydrogen storage as shown in Figure 8a. This is not surprising given that the overall porosity does not alter significantly on reactivation as discussed above. However, re-activation of sample C1-1/4-600 at 700$^o$C and a hydrochar/KOH ratio of 1/4 (yielding sample AC1(1/4-700)) increases the total hydrogen

uptake (Figure 8a) especially at 20 bar (Table 3). The uptake at 20 bar increases from 4.9 to 6.4 wt%. Re-activation of sample C4-1/2-700 at 600$^{o}$C and a hydrochar/KOH ratio of 1/2 (yielding sample AC4(1/2-600)) causes a decrease in hydrogen uptake (Figure 8b), with the uptake at 20 bar reducing from 4.2 wt% to 3.9 wt%. This is an interesting result given that the overall porosity (total surface area, pore volume and proportion of microporosity) remain unchanged after re-activation. The decrease in hydrogen uptake appears to be related to a change in micropore size distribution. As shown in Figure 6b, the micropore size distribution broadens significantly despite the unchanging overall textural properties or proportion of microporosity. This suggests that the broadening of micropore size from 0.9 nm to 1.1 nm (with $L_0$ value increasing from 1.0 nm to 1.4 nm) creates pores that are less effective in hydrogen storage. This result indicates the sensitivity of hydrogen uptake in carbons to the pore size even within the micropore range. On the other hand re-activation of sample C4-1/2-700 at 700$^{o}$C and a hydrochar/KOH ratio of 1/4 to yield sample AC4(1/4-700) significantly increases the hydrogen uptake (Figure 8b). The uptake at 20 bar increases from 4.2 wt% to 5.7 wt%. It is however noteworthy that the increase in hydrogen uptake (i.e., 36%) is much lower that the 92% increase in surface area. This may be explained by the fact that much of the increase in surface area is related to the creation of larger (ca. 2 nm) micropores that are less efficient in hydrogen storage.

A first glance at Figure 7 and 8 and the data given in Table 2 and 3 shows that: a) the higher the surface area, the greater the hydrogen uptake (Figure 7a and Figure 8), b) activated carbons with comparable textural characteristics (e.g., those synthesized at 700$^{o}$C and a hydrochar/KOH ratio of 1/4) exhibit similar hydrogen uptakes (Figure 7b) regardless of the hydrochar used as precursor and c) re-activation may be used to further enhance the hydrogen uptake of the carbons. The hydrogen uptake of the activated and reactivated carbons is plotted as a function of surface area in Figure 9 to explore variation in hydrogen storage

density. A linear relationship is obtained for the activated carbons (slope = $2.44\times10^{-3}$ ± 0.00006 wt%/($m^2$ $g^{-1}$) = 12.2 ± 0.3 μmol $H_2$ $m^{-2}$), except for C4-1/2-700 (16.4 μmol $m^{-2}$). All the carbons clearly outperform the Chahine rule (slope = 10 μmol $H_2$ $m^{-2}$),[37] represented by the solid line in Figure 9. We have previously observed similar behaviour for KOH activated carbide-derived carbons (11.8 ± 0.7 μmol $H_2$ $m^{-2}$)[38] and KOH activated zeolite-templated carbons (10.7 ± 0.8 μmol $H_2$ $m^{-2}$)].[39] It should be noted that Gogotsi et al. have already pointed out that the Chahine rule is not generally valid.[40] The values of hydrogen storage density (i.e., uptake per surface area) obtained for the hydrochar-based activated carbons are superior to those reported in the literature for: a) KOH activated CDCs (10 ± 0.7 μmol $H_2$ $m^{-2}$) and $CO_2$ activated CDCs (9 ± 0.1 μmol $H_2$ $m^{-2}$) (measured at -196ºC and 60 bar),[40] b) different carbon nanostructures consisting of activated carbons and CNTs (9.55 μmol $H_2$ $m^{-2}$) (-196ºC and 60 bar)[31] and activated carbons, SWNTs, SWNHs, GCFs (11.75 μmol $H_2 \cdot m^{-2}$) (-196ºC and 20 bar)[34] and c) chemically activated carbons obtained from anthracite (9 ± 0.1 μmol $H_2$ $m^{-2}$) (-196ºC and 20 bar).[36] These can be more clearly seen if the hydrogen uptake is plotted as a function of surface area for all the materials mentioned above (Figure S3, Supporting Information).

The case of sample C4-1/2-700, which exhibits the highest storage density (i.e., ratio of hydrogen storage per surface area) is remarkable; the sample does not fit the linear relationship existing for the rest of the activated carbons (Figure 9). The sample possesses the smallest pore size, 0.9 nm according to the DFT pore size distribution, a value which is very similar to that deduced using the Stoeckli equation, i.e., 1.0 nm (Table 2). This result agrees with several previous reports, which show that pores < 1nm are most efficient for hydrogen storage.[40-48] As discussed above, reactivation of this sample reduces the hydrogen uptake capacity due to an increase in pore size from 0.9 to 1.1 nm even though the overall surface area, pore volume and microporosity remain unchanged. Whilst the hydrogen uptake density

of the activated carbons is in the range 11.7 to 12.5 μmol $H_2$ $m^{-2}$ at 20 bar and 5.1 to 5.7 μmol $H_2$ $m^{-2}$ at 1 bar the uptake density of sample C4-1/2-700 is much higher at 16.4 and 9.0 μmol $H_2$ $m^{-2}$ at 20 and 1 bar respectively. An increase in micropore size generally causes a decrease in hydrogen uptake density, as illustrated in Tables 2 and 3. The critical influence of the pore size on hydrogen uptake is clearly observed if the hydrogen uptake density (i.e., normalized to surface area) in μmol $H_2 \cdot m^{-2}$ is plotted as a function of the average pore width, $L_0$, as shown in Figure 10. There is a linear decrease in hydrogen uptake density as micropore size increases in the 0.9 to 2 nm range. The higher hydrogen uptake (at 20 bar) of samples X-1/4-700 and Cn-1/4-T compared to C4-1/2-700 despite their larger pore size may be attributed to the compensation effect of their higher surface area. The hydrogen uptake when plotted as a function of the pore volume (Figure S4, Supporting Information) shows a relationship similar to that of surface area (Figure 9). The sample with the smallest value of $L_0$ (i.e., C4-1/2-700) lies above the fitting line, whereas the samples with the largest $L_0$ (i. e., C2-1/4-700 and C3-1/4-800) lie below the fitting line.

With the aim of better understanding the influence of the pore size on the hydrogen adsorption, the isosteric heat of adsorption ($Q_{st}$) was calculated from hydrogen isotherms measured at two temperatures, i.e., -196 and -186ºC. The dependence of the isosteric heat of adsorption on the surface coverage (θ) is given by the Clausius-Clapeyron equation:

$$Qst = - R \left[ \frac{\partial \ln(P)}{\partial (1/T)} \right]_{\theta} \quad (3)$$

where R is the universal gas constant, P the pressure and T the temperature. The plot of the isosteric heat of adsorption as a function of the amount of hydrogen adsorbed for some representative activated carbons is shown in Figure 11. It can be seen that the heat of adsorption decreases at higher hydrogen uptake.[48,49] At low surface coverage (indicative of the hydrogen-surface interaction) the isosteric heat of adsorption reaches a value of ~ 5.8 kJ

$mol^{-1}$ for C2-1/4-700, ~ 8 kJ $mol^{-1}$ for E-1/4-700 and ~ 8.5 kJ $mol^{-1}$ for C4-1/2-700. In all cases $Q_{st}$ decreases to between 3 and 3.9 kJ $mol^{-1}$ at high surface coverage. The higher value of $Q_{st}$ for C4-1/2-700 in comparison with that for C2-1/4-700 and E-1/4-700 confirms that the carbon-hydrogen interaction is greater as the micropore size diminishes. On the other hand, although C2-1/4-700 and E-1/4-700 possess similar pore size distribution, their $Q_{st}$ differ significantly with a higher value for sample E-1/4-700. Both samples exhibit the same hydrogen uptake (5.6 wt%) although E-1/4-700 has slightly lower surface area (2252 $m^2$ $g^1$) compared to C2-1/4-700 (2370 $m^2$ $g^1$). Although our data suggest that porosity is the overriding factor in determining the hydrogen storage capacity, it is worthwhile to note that a comparison between E-1/4-700 (5.2% oxygen) and C2-1/4-700 (7.1% oxygen) suggests that for carbons with similar textural properties, the oxygen content may have a role in determining $Q_{st}$. Overall, the $Q_{st}$ values observed here are similar to those of other carbon materials such as Ti-CDCs (8.5 kJ $mol^{-1}$),[40] SWCNs (7.4-7.8 kJ $mol^{-1}$),[50] zeolite-templated carbons (8.2 kJ $mol^{-1}$)[48] and higher than those of most activated carbons (4 - 6.5 kJ $mol^{-1}$)[51-54] and MOFs (3 - 5.6 kJ $mol^{-1}$).[51,55,56] This higher interaction between hydrogen and the surface of the activated carbons reported here in comparison with other activated carbons would explain the higher hydrogen uptake density per unit surface area of these materials compared to those of other activated carbons.

## 4. Conclusions

In summary, we have demonstrated that hydrochar materials prepared by hydrothermal carbonization of a variety of organic materials (saccharides, biomass or furfural) constitute excellent precursors for the synthesis of activated carbons (via chemical activation), which exhibit highly developed porosity made up of super-micropores. These activated carbons have high surface area (> 2000 $m^2$ $g^{-1}$), large pore volumes (~ 1 $cm^3$ $g^{-1}$) and narrow micropore size distributions in the 0.8 - 2 nm range. Moreover, it has been shown that the

pore characteristics (i.e., pore size and surface area) can be modulated by varying the activation conditions (i.e., activation temperature and the amount of KOH). Re-activation of the activated carbons may be used to further fine-tune the porosity of the carbons. The hydrochar-derived activated carbons exhibit high hydrogen uptakes, up to 6.4 wt%. Furthermore, the interaction between carbon and hydrogen molecules is strong, as shown by the isosteric heat of adsorption of between 6 and 8.5 kJ $mol^{-1}$. This strong interaction leads to higher specific hydrogen uptakes (in the range 11.7 – 16.4 μmol $H_2$ $m^{-2}$) than those normally obtained for activated carbons. These uptake characteristics, and the fact that the precursors used are readily available, and can be obtained via "green" and sustainable processes (e.g., hydrothermal carbonization) make the present activated carbons promising candidates for hydrogen storage. More generally, our findings provide further evidence that pores < 1nm are the most efficient for hydrogen storage.

**Acknowledgement**

M. S. acknowledges the assistance of the Spanish MICINN for the award of a postdoctoral mobility contract.

**References**

1 M. M. Titirici, M. Antonietti, *Chem. Soc. Rev*., 2010, **39**, 103.

2 M. Sevilla, A. B. Fuertes, *Chem. Eur. J.,* 2009, **15**, 4195.

3 M. Sevilla, A. B. Fuertes, *Carbon,* 2009, **47**, 2281.

4 X-L. Li, T-J. Lou, X-M. Sun, Y-D. Li, *Inorg. Chem.,* 2004, **43**, 5442-5444.

5 M. Zheng, J. Cao, X. Chang, J. Wang, J. Liu, X. Ma, *Mater. Lett.,* 2006, **60**, 2991.

6 M. M. Titirici, M. Antonietti, A. Thomas, *Chem. Mater*., 2006, **18**, 3808.

7 X. Sun, J. Liu, Y. Li, *Chem. Eur. J.,* 2006, **12**, 2039.

8 C. Wang, C. Xiangfeng, W. Mingmei, *Sens. Actuators B: Chem*., 2007, **120**, 508.

9 X. Sun, Y. Li, *Chem. Int. Ed.,* 2004, **43**, 597.

10 P. Kim, J. B. Joo, W. Kim, J. Kim, I. K. Song, J. Yi, *Catal. Letter,* 2006, **112**, 213.

11 M. M. Titirici, A. Thomas, M. Antonietti, *Adv. Funct. Mater.,* 2007, **17**, 1010.

12 M. M. Titirici, A. Thomas, M. Antonietti, *J. Mater. Chem.,* 2007, **17**, 3412.

13 J. B. Joo, Y. J. Kim, W. Kim, P. Kim, J. Yi, *Catal. Commun.,* 2008, **10**, 267.

14 W. Qiao, L. Ling, Q. Zha, L. J. Liu, *Mater. Sci*., 1997, **32**, 4447.

15 D. Lozano-Castelló, M. A. Lillo-Róndeas, D. Cazorla-Amorós, A. Linares-Solano, *Carbon,* 2001, **39**, 741.

16 M. Wu, Q. Zha, J. Qiu, Y. Guo, H. Shang, A. Yuan, *Carbon,* 2004, **42**, 205.

17 K. Kierzek, E. Frackowiak, G. Lota, G. Gryglewicz, J. Machnikowski, *Electrochim. Acta*, 2004, **49**, 515.

18 M. J. Illán-Gómez, A. García-García, C. Salinas-Martínez de Lecea, A. Linares-Solano, *Energ. Fuel*., 1996, **10**, 1108.

19 D. Lozano-Castelló, D. Cazorla-Amorós, A. Linares-Solano, D. F. Quinn, *Carbon,* 2002, **40**, 989.

20 A. Linares-Solano, D. Lozano-Castelló, M. A. Lillo-Ródenas, D. Cazorla-Amorós, in Chemistry and Physics of Carbon (Ed. L. R. Radovic), CRC Press, 2007, vol. 30.

21 M. M. Dubinin, *Carbon*, 1989, **27**, 457.

22 F. Stoeckli, L. Ballerini, *Fuel,* 1991, **70**, 557.

23 M. A. Lillo-Ródenas, J. Juan-Juan, D. Cazorla-Amorós, A. Linares-Solano, *Carbon,* 2004, **42**, 1371.

24 P. Ehrburger, A. Addoun, F. Addoun, J. B. Donnet, *Fuel,* 1986, **65**, 1447.

25 M. A. Lillo-Ródenas, D. Cazorla-Amorós, A. Linares-Solano, *Carbon,* 2003, **41**, 267.

26 H. Teng, L-Y. Hsu, *Ind. Eng. Chem. Res.,* 1999, **38**, 2947.

27 F. Stoeckli, *Russian Chem. Bull. Int. Ed.,* 2001, **50**, 2265.

28 F. Stoeckli, A. Guillot, A. M. Slasli, D. Hugi-Cleary, *Carbon,* 2002, **40**, 211.

29 Y. Guo, S. Yang, K. Yu, J. Zhao, Z. Wang, H. Xu, *Mater. Chem. Phys.,* 2002, **74**, 320.

30 H. Sütcü, H. Demiral, *J. Anal. Appl. Pyrolysis*, 2009, **84**, 47.

31 B. Panella, M. Hirscher, S. Roth, *Carbon,* 2005, **43**, 2209.

32 Y. Kojima, Y. Kawai, A. Koiwai, N. Suzuki, T. Haga, T. Hioki, K. J. Tange, *Alloys Compd*., 2006, **421**, 204.

33 K. M. Thomas, *Catal. Today,* 2007, **120**, 389.

34 W-C. Xu, K. Takahashi, Y. Matsuo, Y. Hattori, M. Kumagai, S. Ishiyama, K. Kaneko, S. Iijima, *Int. J. Hydrogen Energy*, 2007, **32**, 2504.

35 K. Xia, Q. Gao, S. Song, C. Wu, J. Jiang, J. Hu, L. Gao, *Int. J. Hydrogen Energy,* 2008, **33**, 116.

36 M. Jordá-Beneyto, F. Suárez-García, D. Lozano-Castelló, D. Cazorla-Amorós, A. Linares-Solano, *Carbon,* 2007, **45**, 293.

37 E. Poirier, R. Chahine, T. K. Bose, *Int. J. Hydrogen Energy*, 2001, **26**, 831.

38 M. Sevilla, R. Foulston, R. Mokaya, *Energy Environ. Sci.,* 2010, **3**, 223.

39 M. Sevilla, N. Alam, R. Mokaya, *J. Phys. Chem. C*, 2010, **114**, 11314.

40 Y. Gogotsi, C. Portet, S. Osswald, J. M. Simmons, T. Yildirim, G. Laudisio, J. E. Fischer, *Int. J. Hydrogen Energy*, 2009, **34**, 6314.

41. Y. Xia, G. S. Walker, D. M. Grant, R. Mokaya, *J. Am. Chem. Soc*., 2009, **131**, 16493.

42 S. K. Bhatia, A. L. Myers, *Langmuir*, 2006, **22**, 1688.

43 M. G. Nijkamp, J. E. M. J. Raaymakers, A. J. van Dillen, K. P. de Jong, *Appl. Phys. A*, 2001, **72**, 619.

44 A. Pacula, R. Mokaya, *J. Phys. Chem. C*, 2008, **112**, 2764.

45 N. Texier-Mandoki, J. Dentzer, T. Piquero, S. Saadallah, P. David, C. Vix-Guterl, *Carbon,* 2004, **42**, 2744.

46 I. Cabria, M. J. López, J. A. Alonso, *Carbon,* 2007, **45**, 2649.

47 Y. Xia, Z. Yang, R. Mokaya, *Nanoscale*, 2010, **2**, 639.

48 Z. Yang, Y. Xia, R. Mokaya, *J. Am. Chem. Soc*., 2007, **129**, 1673.

49 G. Srinivas, Y. Zhu, R. Piner, N. Skipper, M. Ellerby, R. Ruoff, *Carbon,* 2010, **48**, 630.

50 A. Ansón, M. A. Callejas, A. M. Benito, W. K. Maser, M. T. Izquierdo, B. Rubio, J. Jagiello, M. Thommes, J. B. Parra, M. T. Martínez, *Carbon,* 2004, **42**, 1243.

51 B. Schmitz, U. Müller, N. Trukhan, M. Schubert, G. Férey, M. Hirscher, *Chem. Phys. Chem.,* 2008, **9**, 2181.

52 L. Zhou, Y. Zhou, Y. Sun, *Int. J. Hydrogen Energy,* 2004, **29**, 475.

53 P. Bénard, R. Chahine, *Langmuir,* 2001, **17**, 1950.

54 X. B. Zhao, B. Xiao, A. J. Fletcher, K. M. Thomas, *J. Phys. Chem. B,* 2005, **109**, 8880.

55 B. Panella, M. Hirscher, H. Pütter, U. Müller, *Adv. Funct. Mater.,* 2006, **16**, 520.

56 E. Poirier, A. Dailly, *Nanotechnology,* 2009, **20**, 204006 (6pp).

**Table 1.** Elemental analysis of hydrochar precursors and activated carbons.

| Sample | C [%] | H [%] | O [%] | (O/C) [a] | (H/C) [a] |
|---|---|---|---|---|---|
| C | 69.5 | 6.2 | 24.4 | 0.263 | 1.076 |
| S | 68.8 | 6.6 | 24.6 | 0.269 | 1.151 |
| C1-1/4-600 | 86.9 | 1.2 | 11.5 | 0.099 | 0.163 |
| C2-1/4-700 | 92.2 | 0.6 | 7.1 | 0.057 | 0.072 |
| C3-1/4-800 | 95.0 | 0.2 | 4.4 | 0.035 | 0.030 |
| C4-1/2-700 | 85.8 | 1.7 | 11.9 | 0.103 | 0.239 |
| G-1/4-700 | 92.8 | 0.6 | 6.4 | 0.052 | 0.074 |
| S-1/4-700 | 91.9 | 0.5 | 7.3 | 0.059 | 0.065 |
| E-1/4-700 | 94.1 | 0.5 | 5.2 | 0.041 | 0.067 |
| F-1/4-700 | 93.0 | 0.6 | 6.1 | 0.049 | 0.072 |

[a] Atomic ratio

**Table 2.** Textural properties, activation process yield and hydrogen uptake capacity of activated carbons.

| Sample | Yield [%] [a] | Surface area [$m^2$ $g^{-1}$] | Pore volume [$cm^3$ $g^{-1}$] | Microporosity | | $E_0$ [kJ $mol^{-1}$] | $L_0$ [nm] | PSD maximum [nm] [b] | $H_2$ uptake [wt %] [c] | $H_2$ uptake density [μmol $H_2$ $m^{-2}$] [c] |
|---|---|---|---|---|---|---|---|---|---|---|
| | | | | $S_{micropore}$ [$m^2$ $g^{-1}$] | $V_{micropore}$ [$cm^3$ $g^{-1}$] | | | | | |
| C1-1/4-600 | 42 | 2014 | 0.94 | 1843 | 0.81 | 18.3 | 1.6 | 1.2 | 4.9 (2.3) | 12.2 (5.7) |
| C2-1/4-700 | 34 | 2370 | 1.08 | 2201 | 0.96 | 17.3 | 1.8 | 1.2/1.5 | 5.6 (2.5) | 11.8 (5.3) |
| C3-1/4-800 | 33 | 2047 | 0.98 | 1707 | 0.74 | 16.5 | > 2.0 | 1.2/2.0 | 4.8 (2.1) | 11.7 (5.1) |
| C4-1/2-700 | 48 | 1283 | 0.68 | 1229 | 0.57 | 22.3 | 1.0 | 0.9 | 4.2 (2.3) | 16.4 (9.0) |
| G-1/4-700 | 43 | 2121 | 1.00 | 2012 | 0.91 | 17.8 | 1.7 | 1.2/1.5 | 5.3 (2.4) | 12.5 (5.7) |
| S-1/4-700 | 37 | 2194 | 1.01 | 2082 | 0.92 | 18.0 | 1.6 | 1.2/1.5 | 5.4 (2.4) | 12.3 (5.5) |
| E-1/4-700 | 36 | 2252 | 1.03 | 2088 | 0.91 | 17.6 | 1.7 | 1.2/1.5 | 5.6 (2.5) | 12.4 (5.6) |
| F-1/4-700 | 34 | 2179 | 1.03 | 2067 | 0.94 | 18.3 | 1.6 | 1.2/1.5 | 5.4 (2.5) | 12.4 (5.7) |

[a] (g of activated carbon/100g hydrochar). [b] Maxima of the pore size distribution calculated by NLDFT. [c] Hydrogen uptake capacity at -196ºC and 20 bar; the hydrogen uptake capacity at -196ºC and 1 bar is indicated in parenthesis.

**Table 3.** Textural properties, reactivation process yield and hydrogen uptake capacity of doubly activated carbons.

| Sample | Surface area [$m^2$ $g^{-1}$] | Pore volume [$cm^3$ $g^{-1}$] | Microporosity | | $E_0$ [kJ $mol^{-1}$] | $L_0$ [nm] | PSD maximum [nm] [b] | $H_2$ uptake [wt %] [c] | $H_2$ uptake density [μmol $H_2$ $m^{-2}$] [c] |
|---|---|---|---|---|---|---|---|---|---|
| | | | $S_{micropore}$ [$m^2$ $g^{-1}$] | $V_{micropore}$ [$cm^3$ $g^{-1}$] | | | | | |
| C1-1/4-600 | 2014 | 0.94 | 1843 | 0.81 | 18.3 | 1.6 | 1.2 | 4.9 (2.3) | 12.2 (5.7) |
| AC1 (1/4-600) | 1853 | 0.87 | 1676 | 0.73 | 18.0 | 1.6 | 1.2 | 5.1 (2.2) | 13.8 (5.9) |
| AC1 (1/4-700) | 2722 | 1.23 | 2502 | 1.06 | 16.8 | 2.0 | 1.2/2.0 | 6.4 (2.5) | 11.7 (4.6) |
| C4-1/2-700 | 1283 | 0.68 | 1229 | 0.57 | 22.3 | 1.0 | 0.9 | 4.2 (2.3) | 16.4 (9.0) |
| AC4 (1/2-700) | 1280 | 0.64 | 1197 | 0.53 | 19.1 | 1.4 | 1.1 | 3.9 (1.6) | 15.2 (6.3) |
| AC4 (1/4-700) | 2469 | 1.18 | 2254 | 0.96 | 16.8 | 2.0 | 1.2/2.0 | 5.7 (2.2) | 11.5 (4.5) |

[a] (g of activated carbon/100g hydrochar). [b] Maxima of the pore size distribution calculated by NLDFT. [c] Hydrogen uptake capacity at -196ºC and 20 bar; the hydrogen uptake capacity at -196ºC and 1 bar is indicated in parenthesis.

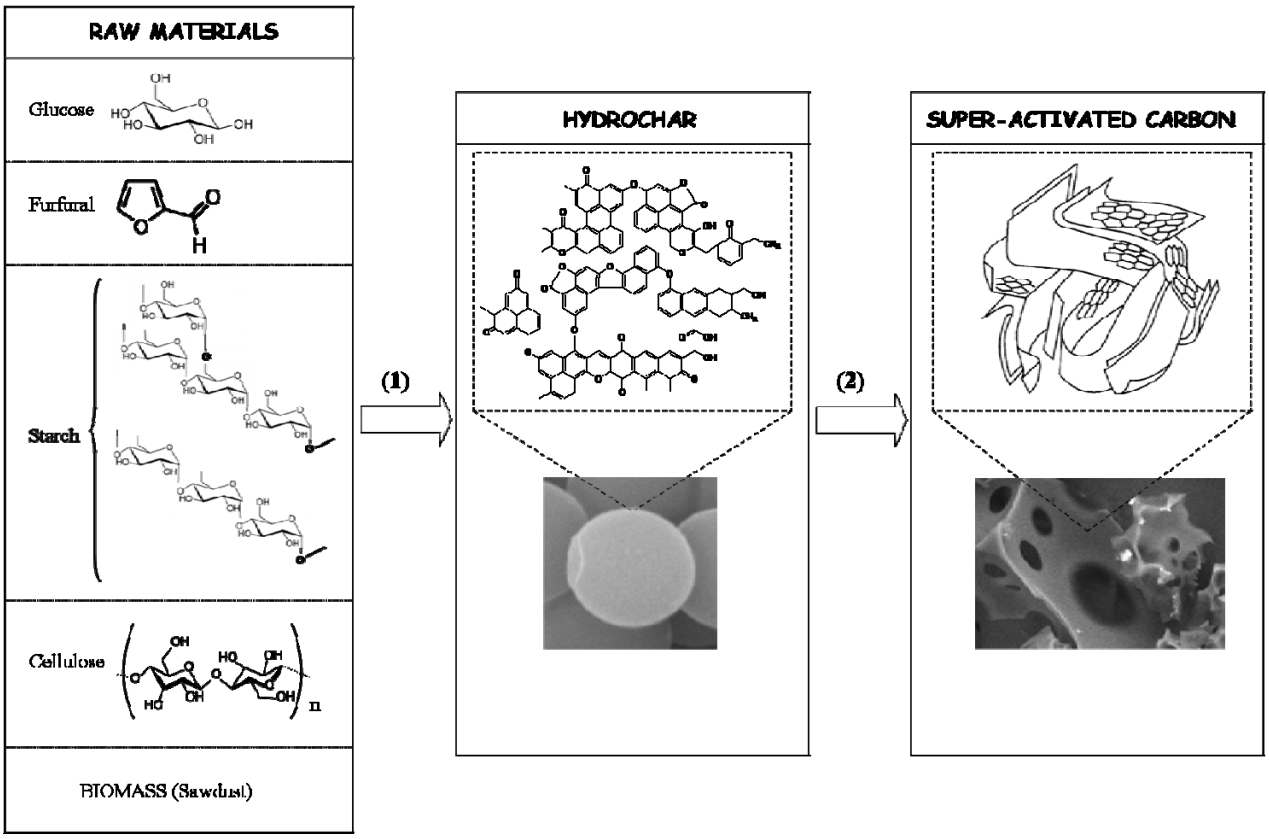


**Figure 1.** Schematic illustration of the overall synthesis procedure for the activated carbons: (1) hydrothermal carbonization at 230 – 250ºC for 2 h, and (2) chemical activation with KOH.

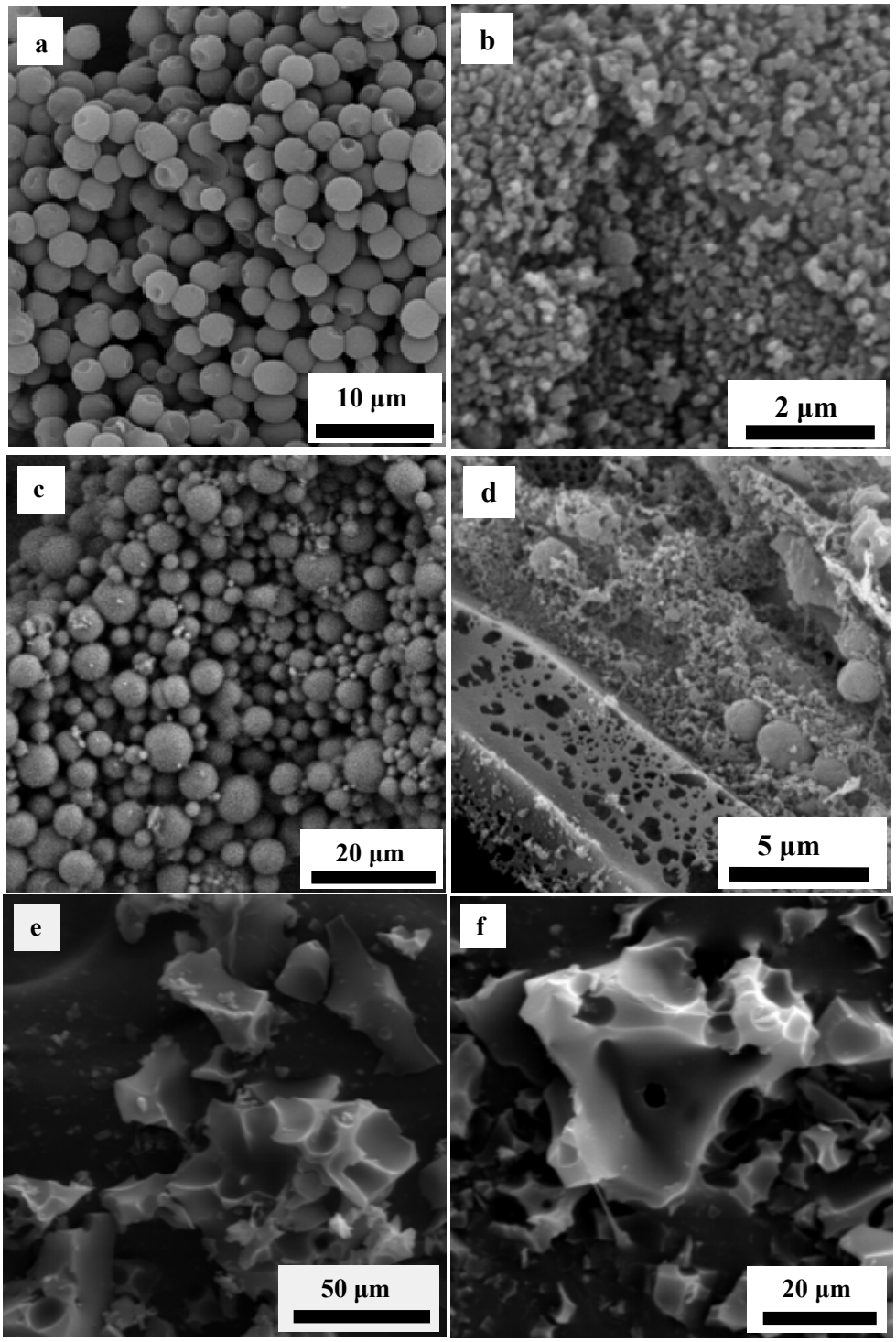


**Figure 2.** SEM images of (a-d) hydrochar materials derived from (a) glucose (G), (b) cellulose (C), (c) Furfural (F), (d) eucalyptus sawdust (E), and (e-f) activated carbons (e) E-1/4-700 and (f) C1-1/4-600.

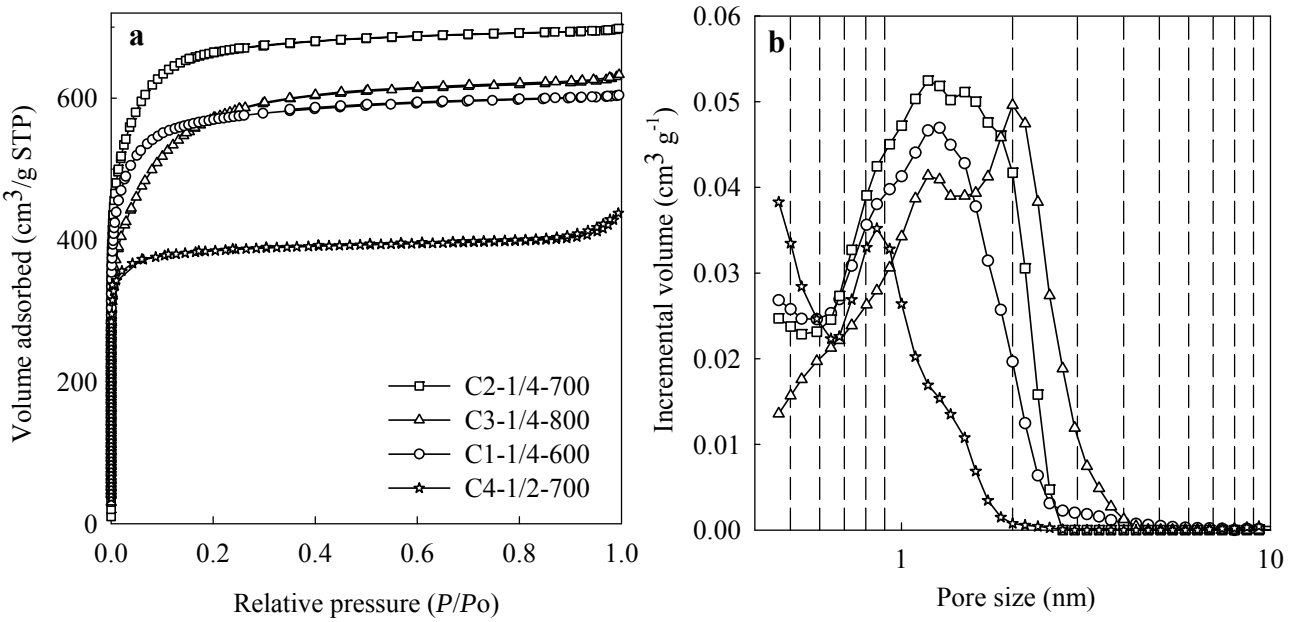


**Figure 3.** (a) Nitrogen sorption isotherms and (b) pore size distributions of activated carbons obtained from cellulose-derived hydrochars following activation at various temperature (600 – 800ºC) and hydrochar/KOH weight ratio (1/2 or 1/4).

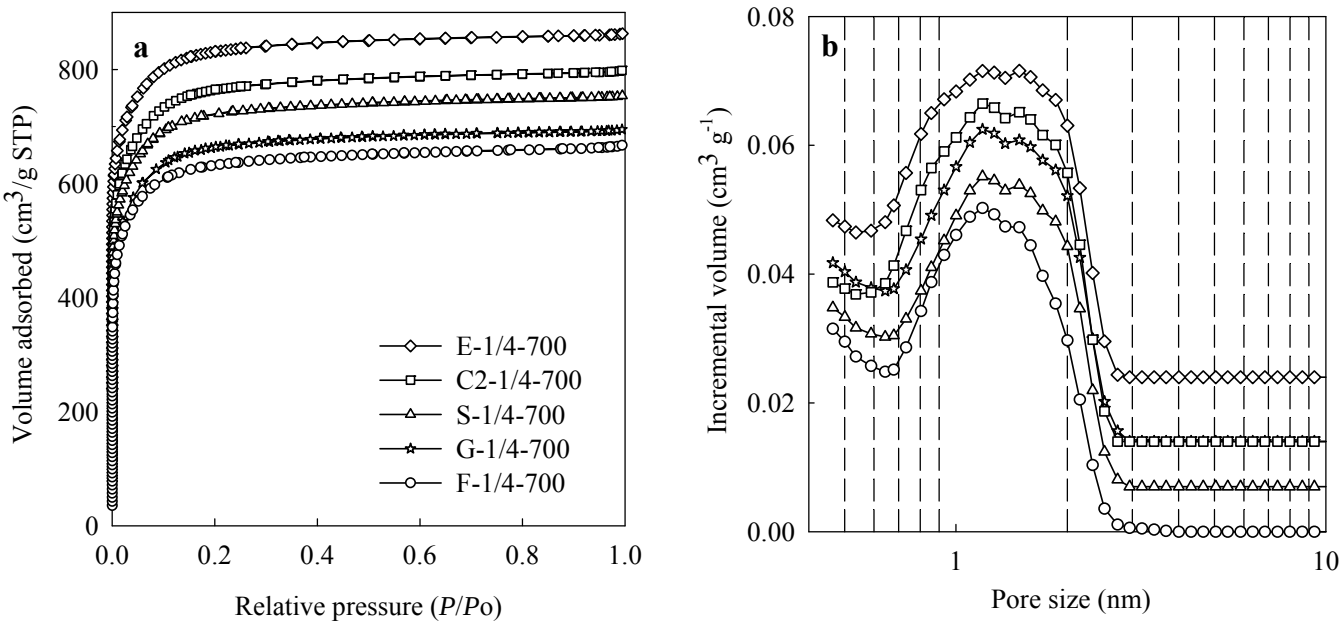


**Figure 4.** (a) Nitrogen sorption isotherms and (b) pore size distributions of activated carbons obtained from various hydrochars following activation at 700ºC and hydrochar/KOH weight ratio of 1/4. For clarity, the isotherms for G-1/4-700, S-1/4-700, C2-1/4-700 and E-1/4-700 are offset (y-axis) by 50, 100, 100 and 200 $cm^3$ $g^{-1}$ respectively, and the PSD curves by 0.007, 0.014, 0.014 and 0.024 $cm^3$ $g^{-1}$ respectively.

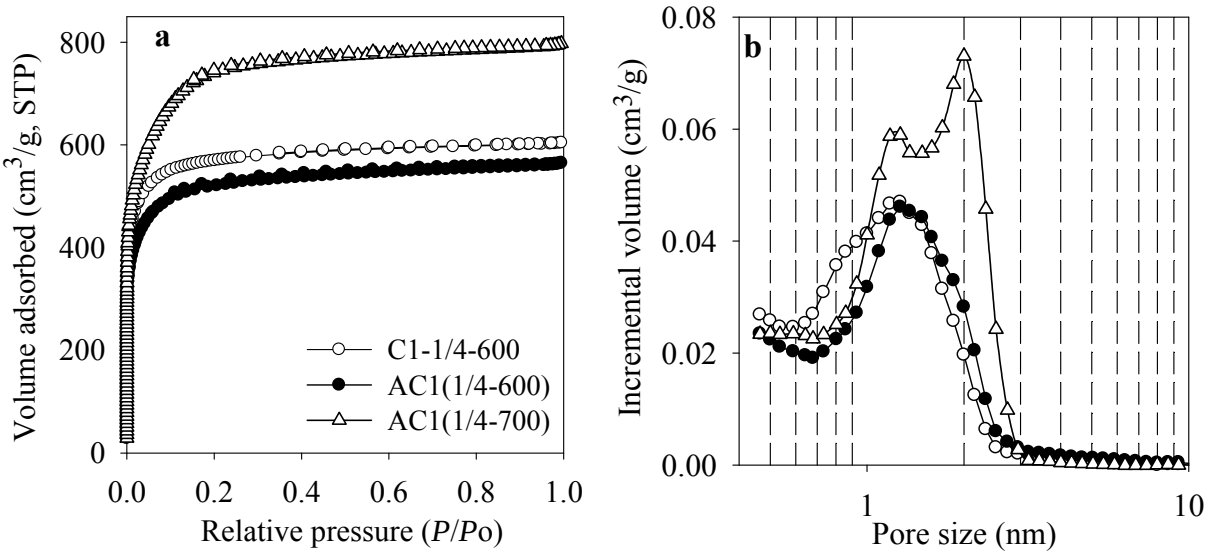


**Figure 5.** (a) Nitrogen sorption isotherms and (b) pore size distributions of activated carbon C1-1/4-600 before and after re-activation at a hydrochar/KOH weight ratio of 1/4 and 600ºC (sample AC1(1/4-600)) or 700°C (sample AC1(1/4-700)).

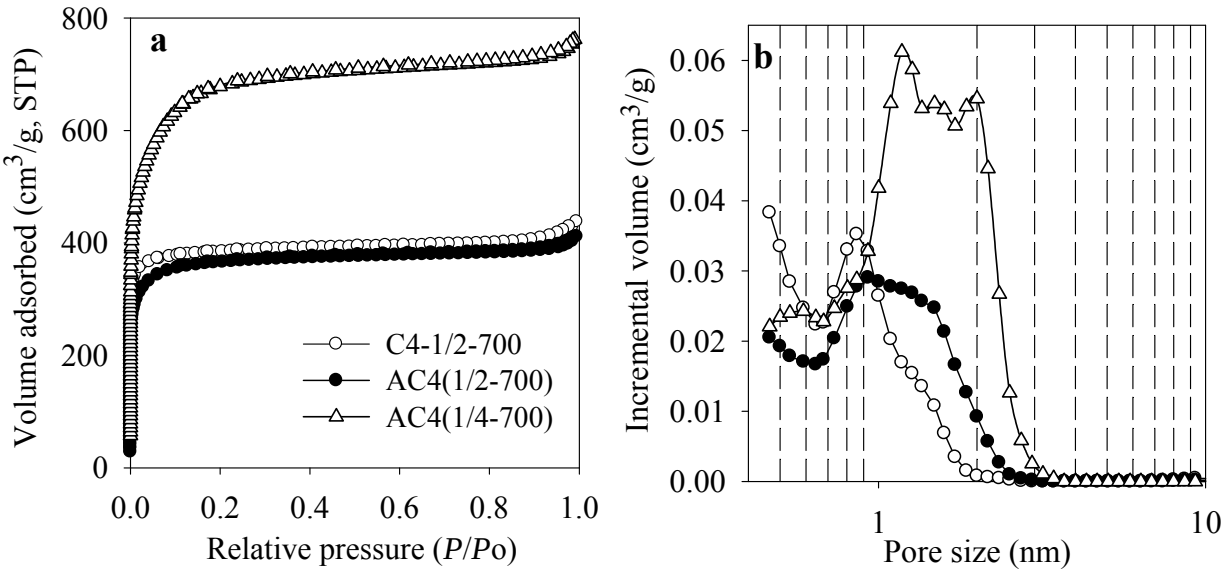


**Figure 6.** (a) Nitrogen sorption isotherms and (b) pore size distributions of activated carbon C4-1/2-700 before and after re-activation at 700ºC and a hydrochar/KOH weight ratio of 1/2 (sample AC4(1/2-600)) or 1/4 (sample AC4(1/4-700)).

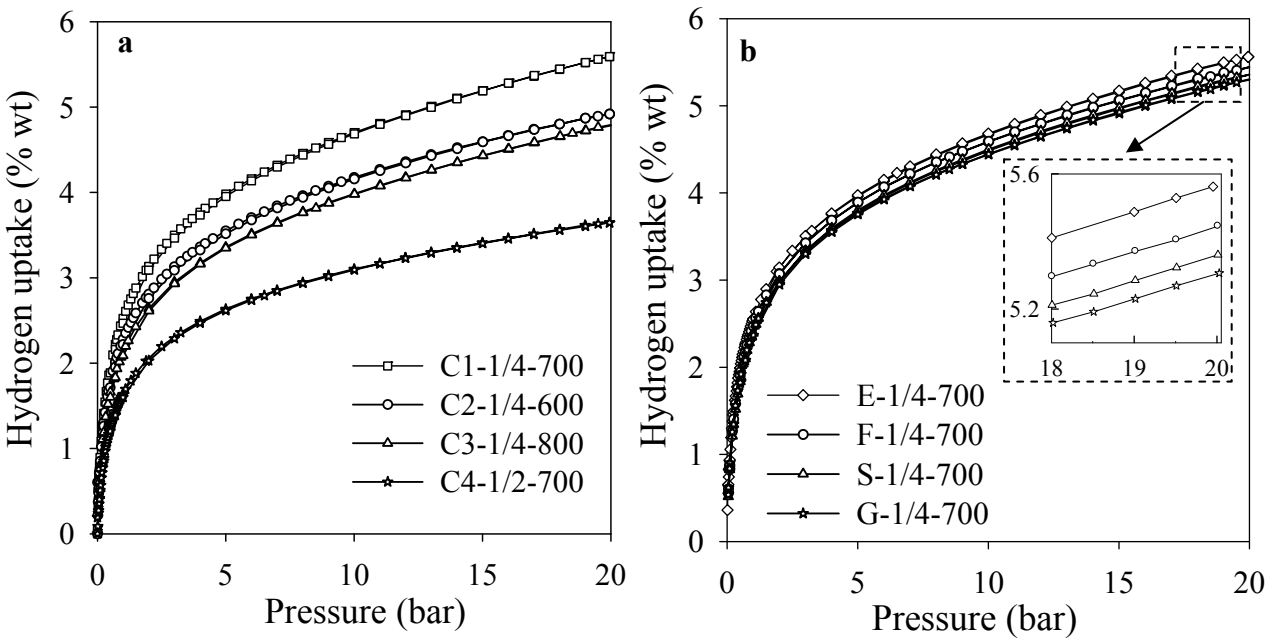


**Figure 7.** Hydrogen uptake isotherms at -196ºC for activated carbons (a) prepared from cellulose-derived hydrochar under various activation conditions, and (b) prepared from various hydrochar materials via activation at 700$^{o}$C and hydrochar/KOH ratio of 1/4. Inset in (b) shows hydrogen uptake at high pressure.

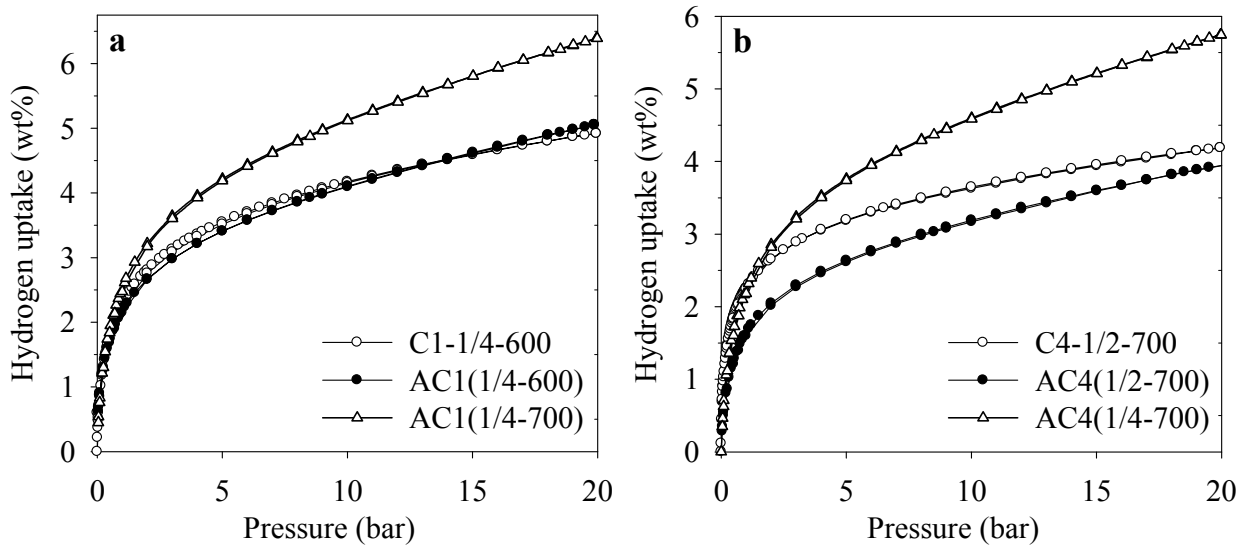


**Figure 8.** Hydrogen uptake isotherms at -196ºC for activated and re-activated carbons; (a) activated carbon C1-1/4-600 before and after re-activation at a hydrochar/KOH weight ratio of 1/4 and 600ºC (sample AC1(1/4-600)) or 700ºC (sample AC1(1/4-700)), and (b) prepared from cellulose-derived hydrochar under various activation conditions, and (b) activated carbon C4-1/2-700 before and after re-activation at 700ºC and a hydrochar/KOH weight ratio of 1/2 (sample AC4(1/2-600)) or 1/4 (sample AC4(1/4-700)).

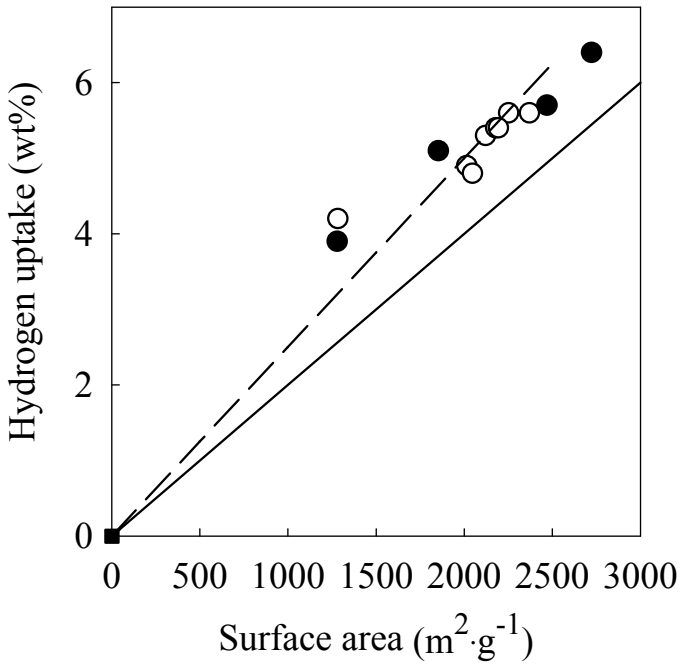


**Figure 9.** Correlation between hydrogen uptake capacity and surface area of activated (○) and re-activated (●) carbons. The solid line corresponds to the Chahine rule and the dotted lines to the fitting of the experimental points to a line which passes through the axes-origin.

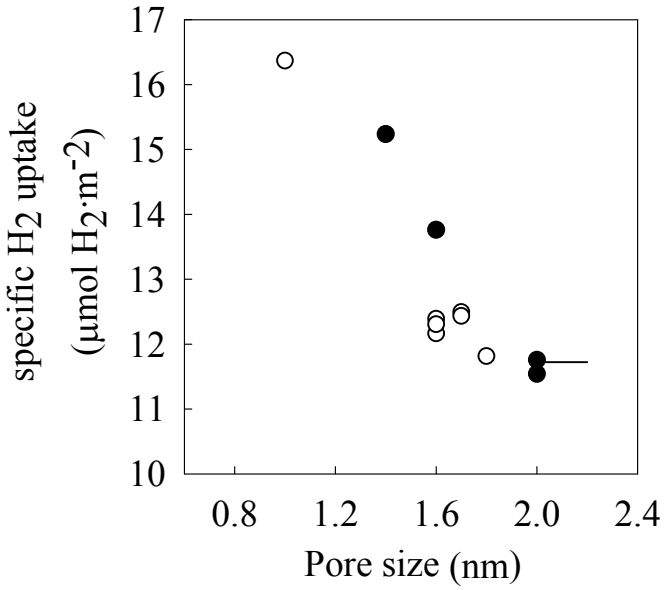


**Figure 10.** Plot of specific hydrogen uptake (in μmol $H_2$ $m^{-2}$) as a function of pore size for the activated (○) and re-activated (●) carbons (sample C3-1/4-800 is represented by a line since $L_0$ > 2 nm).

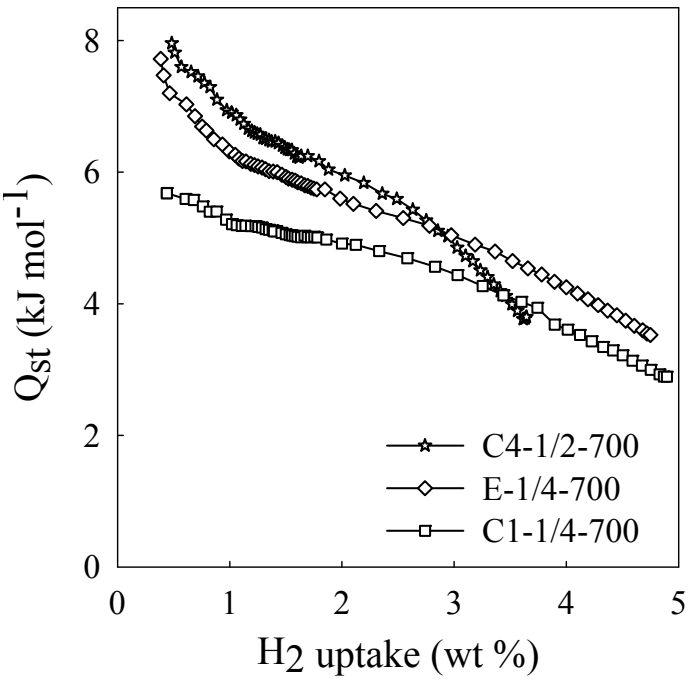


**Figure 11.** Evolution of the isosteric heat of hydrogen adsorption ($Q_{st}$) as a function of hydrogen uptake.